Charge Localization induced Tunable Thermopower in ZnSb Intercalated Polyaniline:CSA Flexible Films

Anmol Sharma[1,2], Nagendra Singh Chauhan[1*], Masako Nishimagi[3] and Takao Mori[1,2*]

[1]Center for Materials Nanoarchitectonics (WPI-MANA), National Institute for Materials Science (NIMS), Namiki 1-1, Tsukuba, 305-0044, Japan.
[2]Graduate School of Pure and Applied Sciences, University of Tsukuba, 1-1-1 Tennodai, Tsukuba, Ibaraki 305-8573, Japan.
[3]ZACROS Corporation Ltd. Tokyo, 112-0002, Japan.

Abstract

Modulating doping levels and nanofillers blending has facilitated optimization of electrical properties in polymeric nanocomposite films for thermoelectric applications. Herein we report, free-standing flexible films of PANI:CSA/ZnSb polymer nanocomposites, with varying nanofillers ZnSb ratios, to realize charge localization induced enhancement in power factor (≈ 10 times) and thermopower (≈ 6 times) within the protonated PANI:CSA. Le Bail refinement of the XRD pattern reveals lattice expansion and reoriented chain conformation in the pseudo-orthorhombic PANI structure due to ZnSb intercalation. The thermopower, enhanced to ≈ 50 μV/K at room temperature, was tunable due to the suppressed bipolaronic states and associated charge localization, resulting in an improved power factor of ≈ 10 μW/m·K^2 . The synthesized polymeric films exhibit excellent mechanical durability, retaining ~90% of their electrical conductivity after 2000 bending cycles. A flexible thermoelectric generator (FTEG) fabricated using six PANI:CSA/70 wt.% ZnSb films produced an output voltage of ~0.9 mV on a human wrist and ~6.7 mV under a temperature gradient of ~50 K, highlighting prospects of charge localization in improving the low and smeared Seebeck response in conducting polymers like PANI and their potential for wearable thermoelectric energy harvesting applications.

Keywords – *Thermoelectrics; Polyaniline; Localization; Intercalation; Conducting Polymers*

---

[*] CHAUHAN.NagendraSingh@nims.go.jp, MORI.Takao@nims.go.jp

1. Introduction. Amidst rising energy demand globally and depleting natural resources, thermoelectric (TE) energy harvesting is emerging as a promising green technology that enables efficient conversion of waste heat energy into electricity. As a sustainable approach to enhance the efficacy of thermal energy conversion, TE applications are expanding to enable the harnessing of low-grade heat sources accessible at dynamic surfaces such as human body, and portable devices operating at the microwatt scale.[1,2] In this context, polymeric TE electronic materials have shown great prospects for flexible and wearable applications, with ongoing research aimed towards optimizing their electronic transport properties.[3,4] For decoupling the inversely related Seebeck coefficient (S) and electrical conductivity (σ), various polymer engineering approaches aims towards maximizing the power factor ($S^2\sigma$).[1,3–5] These approaches typically includes (i) precise control of oxidation level/doping through electrochemical methods; (ii) use of secondary dopants (with organic protic acids such as HCl, H_2SO_4, $HClO_4$, CSA) to improve morphology and increase polarons/bipolarons;[6,7] and (iii) formation of polymer nanocomposites with fillers such as carbon nanomaterials or inorganic nanoparticles.[8–12]

Amongst actively explored conducting polymers, PANI and their derivatives are well recognized for their low cost, tunable energy levels, ease in processability, and near ambient chemical stability.[13,14] Depending on the synthesis conditions, i.e., chemical, electrochemical, or plasma methods, PANI can occur in diverse structural forms and varying degree of crystallinity.[15–18] For TE applications, PANI based nanocomposites having an inherently low thermal conductivity (κ) has garnered much attention owing to their high and tunable σ (ranging from 10^{-13} – 10 S/cm) though simple and often reversible protonic doping.[19–22] The protonation adds positive charges (holes) i.e. *polarons* (singly charged, spin 1/2) and at higher doping levels *bipolarons* (doubly charged, spin 0), onto the conjugated polymer backbone coupling local structural distortion and electrostatically balancing the charges, as shown in Figure 1(a). Amongst studied protic acids (i.e., acid that donates protons, or hydrogen ions, to an aqueous solution), camphor sulfonic acid (CSA), being bulky and hydrophobic, is often preferred as it enables better processability and σ tunability.[19,23] Moreover, higher CSA doping has remained most consistent and effective in degree of protonation per repeat unit,[24–27] typically tuned by molar ratio as indicated in Figure 1(b). Typically, with increasing polaron/bipolaron concentration, hole density (n) increases, promoting delocalization driven by an enhanced overlap between π-orbitals and improved interchain connectivity via π–π stacking. However, higher n from increased doping often results in broadening of transport energy levels, limiting and reducing the $S \sim 10$ μV/K for protonated PANI. Moreover, inhomogeneous polaron distribution coupled with energetically broad and smeared energy distributions, results in a smeared thermopower response for many structural or doping changes, studied in PANI based nanocomposite films hybridized with inorganic materials such as Te[28], PbTe[29], Bi_2Te_3[30], $Bi_{0.5}Sb_{1.5}Te_3$[31], Ag[32,33], Ag_2Te[34], CdS[35], Bi_2Se_3[36], and SnSeS[37].

Developing PANI-based flexible nanocomposite films with improved conductivity and tunable Seebeck coefficient remains challenging due to their heterogeneous structure, complex interchain interactions, and charge transport dominated by localization, hopping, and chain disorder.[38–40] Herein, we investigate the electrical transport behavior in free-standing flexible films of ZnSb nanofillers intercalated PANI:CSA polymer nanocomposites synthesized by solution mixing. Self-supporting films were drop-casted using m-cresol as solvent and subsequent delamination in deionized water.[26] Balancing flexibility in an emeraldine salt state (having intrinsically high σ), the ordered crystalline coordination complexes (ZnSb clusters and metallic islands) surrounded by disordered amorphous regions within the heterogeneous nanocomposites structure, contribute to charge localization.[41] The carrier transport behavior as a function of temperature suggests moderate doping that fits well with the ES-VRH model, accounting for Coulomb interactions and a soft gap in the density of states (DOS).[42,43] The ZnSb nanofillers intercalate between amorphous or semi-ordered domains without significantly disrupting the bulk crystalline regions, as indicated by minimal changes in unit cell parameters. However, ZnSb intercalation while causing lattice expansion and reoriented chain conformation introduces localized states that suppress bipolaron formation and favor polaron transport, thereby enhancing both the thermopower and power factors.

2. Results & Discussion.

2.1 Free-standing Flexible Film, Granular Morphology, and Molecular Configuration.

The synthesis by CSA-doping and ZnSb nanofillers additions in PANI yielded a free-standing flexible dark green film, even for a significantly higher ZnSb content (~ up to 70%) as shown in Figure 2. The co-occurrence of protonation (with CSA) and hybridization with ZnSb nanofiller simultaneously in m-cresol (a polar protic solvent) under stirring and ultrasonication has enabled better dissolution and regulation of the doping level. For cooperative alignment between PANI chains and CSA molecules, m-cresol plays a unique role in enhancing chain ordering and planarity, by strengthening hydrogen bonding with both –SO_3^- group of CSA and protonated nitrogen (–NH^+) of the PANI backbone.[19] Moreover, m-cresol enables coil to extended chain transformation in PANI, thereby promoting planarization, better π–π stacking and interchain connectivity.[44,45] A scheme of our synthesis of PANI:CSA/ZnSb polymeric nanocomposites is presented in Figure 2. The synthesized free-standing films show superior flexibility, with the absence of any cracking on their surfaces for up to 70% ZnSb loading. However, it may be noted that prolonged exposure to oxidizing surroundings was found to degrade PANI chains.

The morphology and microstructure of the representative PANI film surfaces, both with and without ZnSb nanofillers incorporated PANI:CSA, were analyzed by SEM micrographs. In Figure 3(a), the SEM micrograph of PANI:CSA film shows a smooth and dense surface film without any visible cracks and pores. Upon ZnSb nanofiller addition, the polymeric chain retains granular morphology with ZnSb interlinked nanoparticle structures as shown in Figure 3(b – f). Also, at higher ZnSb content (> 60 wt.%), agglomerations of ZnSb nanofillers in the range of ~20-30 μm in size with granular features of size in range ~100 – 500 nm, were observed as shown in Figure 3(e – f). This amorphous or poorly ordered microstructure is representative of the disrupted morphology at high ZnSb loading, which interrupts the conductive polymer network. This morphological disorder likely contributes to the observed decline in electrical conductivity due to reduced carrier mobility and impaired percolation pathways. Elemental mapping through energy-dispersive X-ray microanalysis was simultaneously conducted to investigate the distribution of elements in PANI:CSA and ZnSb-incorporated PANI: CSA films. The relevant elemental maps for Zinc (Zn), Antimony (Sb), Carbon (C), Nitrogen (N), and Sulfur (S), are presented in Figure 3(g – m). As seen in the elemental mapping images of Nitrogen ($-NH^{+}-$), nitrogen was also detected in the ZnSb regions, indicating an interaction between the charged amine group and ZnSb. The polymeric layer thicknesses were also corroborated by the surface profiler and analyzing the transversal cross-section of each polymer with the SEM technique, as shown in Figure 3(n – o). The average thickness of the pristine PANI:CSA, and PANI:CSA/70 wt% ZnSb are 128 μm and 25 μm, respectively. Here, a decrease in the thickness of the nanocomposite film was observed with an increase in ZnSb filler, indicating space-filling and densification of the film. This reduction may be attributed to the occupation of interstitial voids between PANI chains by ZnSb nanoparticles, resulting in higher packing density and reduced local porosity, as also seen in previous studies.[46,47] Furthermore, increasing the ZnSb content while maintaining a fixed amount of PANI:CSA in m-cresol likely reduces the polymer fraction, contributing to the thinner films observed in the PANI:CSA/70 wt.% ZnSb sample during drop-casting.

2.2 Structural Parameters, Semi Crystallinity and Orthorhombic Symmetry. The XRD measurements of the synthesized PANI:CSA shown in Figure 4(a) indicate semi-crystallinity, as evidenced by fewer and broader diffraction peaks, also shown in a magnified view ($2\theta \sim 10 -$ 25°) in Figure 4(b). Although partial crystallinity makes accurate determination of the crystal structure challenging, XRD patterns reveal a broad amorphous region ($2\theta \sim 10 - 25°$), centering around $2\theta \sim 20$ - 22° for synthesized films, which aligns well with previously reported diffraction patterns.[48,49] Nevertheless, the observed XRD patterns are generally consistent with a pseudo-orthorhombic lattice symmetry for crystalline domains of PANI:CSA complex, in which protonated polymer chains and CSA anions pack into a unit cell with approximate lattice parameters $a \approx 7.0 - 7.1$ Å, $b \approx 7.9 - 8.6$ Å, $c \approx 10.4$ A° as reported previously by Pouget et al.[50] The orthorhombic structure (Space group: *Pbca*, 61)[51] of ZnSb and the pseudo-orthorhombic (Space group: *Pc2a*, 32)[48,49] arrangement of PANI is expected to ensure structural compatibility within the composite, minimizing interfacial strain and preserving chemical stability. For conceptual visualization only, molecularly disordered (PANI:CSA) with crystalline (ZnSb) phases are overlayed/merged randomly to attain simulated powder XRD patterns shown alongside based on periodic atomic positions,[52] which surprisingly matches well with the measured XRD patterns. The synthesized unfilled protonated PANI:CSA films display partial order with indexed pseudo-orthorhombic diffraction peaks shown in Figure 4(c) and listed in Table 1, characteristics of PANI semicrystalline structure. The evaluated *d*-spacing for refined structure indicates close agreement with values and (*hkl*) indexation for stretched films, made previously for emeraldine PANI:HCl salt samples.[50]

In the synthesized PANI:CSA, *m*-cresol treatment may be ascribed to an increased π–π *d*-spacing, indicating backbone separation and extended conjugation.[45] As indicated in Figure 4(d), the peak maximum corresponding to the (112) planes, with a *d*-spacing of approximately 4 Å, represents the face-to-face interchain stacking distance between phenyl rings along the conjugated polymer backbones. The low angle shift is indicative of a weaker π–π interaction induced by ZnSb intercalation which increased *d*-spacing by ≈ 1.5 times. For ZnSb hybridized PANI:CSA films, the XRD pattern constitutes a low-angle shift having both broad amorphous regions, and sharp peaks revealing crystalline domains, as shown in Figure 4(a). An alteration in backbone periodicity peaks ($2\theta \approx 10 - 20°$) is clearly observed, which indicates an expanded lamellar stacking or long-range periodicity along the polymer chain (i.e. spacing between doped regions or structural repeats). Moreover, rearrangement of side chains or counterions with ZnSb intercalation may induce disruption in chain stacking (*c*-axis), typically related to peak changes at $2\theta \sim 20 - 22°$ for PANI:CSA complex. Additionally, ZnSb fillers may occupy interstitial spaces within the PANI matrix, reducing the volume of amorphous regions, wherein ZnSb clusters induce an altered stacking order, different internal packing, or domain alignment by disrupting the PANI chains.

The cell parameters and crystallite size of the synthesized film were determined using the Le Bail method, assuming the pseudo-orthorhombic crystal structure (Space group: Pc2a, 32) for the PANI:CSA Complex.[48,49] The ZnSb nanofillers intercalation in polymer nanocomposites is evaluated to result in an expanded interlayer spacings, broadening of existing peaks and peak maxima occurring for new planes i.e. (103) and (211) as indicated in Table 1 and supplementary figure S4 – S8. The refined lattice parameter for pseudo-orthorhombic PANI:CSA Complex, suggest a higher lattice parameter for the synthesized unfilled PANI:CSA films, when compared with stretched films analyzed by Pouget et al.[50] shown in Figure 5(a). Interestingly, despite low angle shift upon ZnSb intercalation when compared to unfilled PANI:CSA for the synthesized films, only marginal changes in pseudo-orthorhombic unit cell parameters were evaluated. Moreover, the average lattice constants (*a*, *b*, *c*) from the crystalline fraction for both pseudo-orthorhombic PANI:CSA complex and orthorhombic ZnSb (Figure 5b) remain mostly unaffected. This may imply an anisotropic structural change, where ZnSb intercalation may occur only along the chain stacking (*c*-axis), causing an anisotropic expansion which averages out due to a marginal shift in *hkl* planes. Moreover, as PANI:CSA complex constitutes large amorphous domains with only smaller proportions of crystalline domains, ZnSb intercalation may only expand or distort the amorphous regions, with minimal penetration into crystalline zones. Thus, we conclude that *d*-spacing for different planes increases locally upon ZnSb intercalation, affecting intermolecular distances largely, while causing marginal distortion to the crystalline domains of PANI:CSA and ZnSb nanofillers, implying structural compatibility.

Although the orthorhombic symmetry match was anticipated to help in attaining an ordered PANI:CSA complex with periodic hybrid layers, to retain the intrinsic electronic structure, preventing degradation or distortion of functional sites, thereby maintaining the charge transport properties essential for TE performance. However, for higher ZnSb content (i.e. >50 %), Sb, ZnS, and ZnO were also identified as additional phases, which is anticipated to be driven by low formation energy of Zn vacancies (V_{Zn}^{2-}). While Zn vacancies typically act as acceptor defects, leading to hole generation (i.e., *p*-type conduction), Zn atoms tendency to form coordination complexes in the presence of strongly acidic sulfonic group (–SO_3H) in organosulfur CSA compounds, may disrupts the π-conjugated system in PANI:CSA complex. The Zn – Sb binary system encompasses two notable thermoelectric materials: the ordered phase ZnSb and the disordered phase $Zn_{13}Sb_{10}$, both having multicenter bonding within Zn_2Sb_2 rhombic structural units. The ZnS and ZnO demixing may electrostatically balance PANI:CSA complex, implying their existence as unreacted clusters when ZnSb nanofillers exceed the percolation threshold or saturation limit of the PANI:CSA matrix. This can convert polarons/bipolarons into neutral or localized states depending on Zn vacancies. Additionally, decomposition of ZnSb phase may interact with charged sites on PANI chains due to co-occurrence of protonation (with CSA) and ZnSb nanofiller hybridization. The alterations in interchain π–π stacking between polymer backbones, in the coherence length (along both the chain direction and perpendicular to it) and the interchain spacing significantly impact the determination of the balance between the localization of electronic charges on individual chains and their delocalization within the 3D-crystalline regions.[41]

2.3 Bonding Interactions, Charge Localization, and Raman Spectra. The coherence length (both along and across the chain direction), and interchain spacing are critical factors influencing the balance between electronic charge localization on a single chain and charge delocalization across three-dimensional crystalline regions. To analyze the chemical interactions between the PANI backbone chain and ZnSb in PANI composites, Raman microscopy was performed on PANI:CSA and its ZnSb nanocomposites to analyze shifts in semi-quinoid and polaron peaks. The pristine PANI spectra (Figure 6) shows distinct peaks corresponding to the emeraldine salt form, including peaks at 415, 513, 578, 717, 810, 1173, 1268, 1340, 1375, 1496, 1590, and 1622 cm^{-1}. The peaks at 415, 513, 578, 717, and 810 cm^{-1} are attributed to *out*-of-plane ring deformation in PANI salt, out-of-plane *C-N-C-H* vibrations, phenazine-type cross-linking, *C-N-C* deformation vibrations, and Benzene ring distortion in emeraldine salt. The peaks at 1173, 1268, 1340, 1375, 1496, 1590, and 1622 correspond to *C-H* bending vibrations of quinonoid (QN) units, *C-N* stretching in semi-QN structures, $C-N^{+\cdot}$ stretching modes of the benzenoid (BZ) and QN cation radicals within delocalized polaronic structures which accounts for conducting-ES form, $C-N^{+\cdot}$ stretching vibrational modes in strongly localized polarons, N-H stretching vibrational modes of QN and BZ rings, *C-C* stretching modes of the QN and BZ rings (delocalized polaron vibration), and phenazine-like crosslinking (*C*=*C* stretching vibrational modes of QN and BZ rings).[25,53,54]

As ZnSb content increases, the peak at 1622 cm^{-1} decreases in intensity and undergoes a blue shift, indicating reduced quinoid units leading to lowered σ. The peaks at 1590 and 1496 cm^{-1} also shift upwards, suggesting increased oxidation, increased localization of polarons, and changes in changes in protonation level. The peak at 1375 cm^{-1} (negligible for pristine PANI-CSA) increases in intensity and shifts to 1378 cm^{-1} (for 70 wt% ZnSb/PANI), indicating the presence of highly localized polaron states trapping the polarons, which is anticipated to reduce both holes concentration and their mobility.[53,54] Additionally, the peak at 1340 cm^{-1} shifts slightly downwards, verifying the presence of delocalization on semi-quinoid units, while the peak at 1268 cm^{-1} shifts down slightly, indicating reduced C-N bonding. Other shifts in peaks (810, 415, 717, 578, and 513 cm^{-1}) further confirm the chemical interaction between ZnSb and PANI:CSA. To analyze the Raman spectra qualitatively, the intensity ratio of specific Raman peaks for PANI:CSA with its 70wt.% ZnSb hybridized counterpart, was evaluated and shown in Table S1 (Supplementary information). The intensity ratio I_1 (i.e. $I_1(1340)/I_1(1590) = 1.28$) & I_3 (i.e. $I_3(1337)/I_3(1600) = 1.05$) corresponds to polaronic delocalization or the doping level, which decreases as ZnSb is introduced, suggesting reduced σ. While the intensity I_2 (i.e. $I_2(1375)/I_2(1590) = 0$ (as no peak was observed) for PANI:CSA) & I_4 (i.e. $I_4(1378)/I_4(1600) = 0.94$) ratios correspond to charge localization. While optimal protonation level in all the synthesized films sustains polaron-bipolarons equilibrium for work function tuning, the positive charge delocalization in the polymer chain imparts enhanced stability of polarons near the anion site.[16]

The X-ray photoelectron spectroscopy (XPS) was conducted to examine the chemical states in the PANI:CSA/70 wt% ZnSb nanocomposite flexible film, as shown in Figure 7. The XPS-wide scan, as shown in Figure 7(a), reveals signature peaks corroborating the presence of C, N, S, Zn, Sb, and O in PANI:CSA/ZnSb polymeric nanocomposites. In Figure 7(b), the sharp C 1*s* peak is shown at ~285 eV, representing different carbon environments in PANI and CSA, while the N 1*s* spectrum corresponds to different nitrogen states in PANI (e.g., neutral, polaron, bipolarons), as shown in Figure 7(c). The superimposed peaks at ~399.3 eV, ~399.95 eV, ~400.85 eV, and ~402.3 eV correspond to imine (=N-), amine (-NH-), polarons, and bipolarons (both being protonated nitrogen (N^+)), respectively. Similar peaks were also shown by Dezhuang et al.[55], for pure PANI and PANI/SWCNT. The S 2*p* spectrum confirms the presence of CSA dopants, showing two peaks at 168 and 169 eV, attributed to the sulfonic group from camphor sulfonic acid, with a binding energy range of ~167–171 eV. The high-resolution Zn 2*p* doublet, with two peaks at ~1023.3 and ~1046.5 eV for Zn $2p_{3/2}$ and Zn $2p_{1/2}$, indicates Zn^{2+} oxidation state. Similarly, the Sb 3*d* spectrum exhibits peaks at ~532.1 and ~540.8 eV for Sb $3d_{5/2}$ and Sb $3d_{3/2}$, which overlap with O 1*s* peaks, showing high intensity and correspond to its presence in PANI:CSA. For comparison, the wide scan survey spectra for PANI:CSA is shown in Figure S12.[56–58] To further elucidate the chemical structure modulated by ZnSb incorporation, high-resolution N 1*s* XPS spectra was deconvoluted for PANI:CSA and PANI:CSA/70 wt.% ZnSb nanocomposite films, respectively. The N 1*s* spectra, as shown in Figure 8(a) & (b), reveal four distinct nitrogen components corresponding to imine (=N–), amine (–NH–), polaronic, and bipolaronic nitrogen species, as also observed previously for deconvoluted N 1*s* spectra.[55]

In pristine PANI:CSA, peaks are observed at ~399.3 eV (=N–), ~399.5 eV (–NH–), ~400.85 eV (polaron), and ~402.9 eV (bipolaron), with corresponding concentration contributions of 21.05%, 30.76%, 27.83%, and 20.36%, respectively. In contrast, the PANI:CSA/70 wt.% ZnSb nanocomposite exhibits the same chemical assignments with slight shifts: ~399.3 eV (=N–), ~399.95 eV (–NH–), ~400.85 eV (polaron), and ~402.3 eV (bipolaron). However, the spectral concentrations are significantly redistributed to 40.78%, 23.95%, 31.97%, and 3.30%, respectively. These deconvoluted peaks reflect a significant decrease in bipolaron content (down to 3.30% from 20.36%) and a marked increase in imine nitrogen (~94% relative rise), suggesting a reduction in the overall oxidation state of the PANI matrix upon ZnSb loading. The suppression of bipolaron states, along with a ~0.6 eV downshift in the bipolaron peak, indicates either their trapping or conversion to polarons. This behavior suggests partial charge localization at the ZnSb–PANI interface, likely induced by interfacial energy barriers or trap states introduced by the ZnSb phase. The moderate increase in polaronic content (N^+ from 27.83% to 31.97%) indicates stabilization of single-charge carriers, while the reduced –NH– peak intensity points to partial deprotonation or chemical restructuring of amine sites under interfacial strain or charge transfer. The overall decrease in the proportion of charged nitrogen species (polaron + bipolaron) relative to total nitrogen supports the observed moderate decline in electrical conductivity. These changes are shown in supplementary Table S2 & S3.

The UV–Vis absorbance spectra of pristine PANI:CSA and the PANI:CSA/70 wt.% ZnSb composite films are shown in Figure 9. The overall absorbance intensity is higher in PANI:CSA across the full spectral range, suggesting a more extended π-conjugated system, whereas the lower absorbance in the composite indicates partial disruption of conjugation upon ZnSb incorporation. In the deep UV region (200–280 nm), PANI:CSA exhibits a sharp absorption band at ~212 nm, which redshifts to ~215.5 nm in the composite. This feature may arise from aromatic ring-related transitions or residual solvent interactions i.e., *m*-cresol.[12] A secondary transition around 253 nm in PANI:CSA, also observed in the composite at ~251.5 nm, is attributed to π–π^* transitions within the benzenoid segments of the polymer backbone. The slight redshift and suppression of these bands in the ZnSb-loaded film suggest local electronic perturbations and possible changes in π-stacking or chain conformation.[12,59,60] In the visible region (300–400 nm), both samples show a polaron–π^* transition, a key signature of charge delocalization in doped PANI. This band appears at ~391 nm for PANI:CSA and shifts to ~397 nm in the composite, accompanied by a noticeable reduction in intensity. These changes may indicate partial localization of polarons and disruption of extended charge transport pathways, consistent with a transition from delocalized to more localized carrier states. In the near-infrared region (800–900 nm), a broad absorption feature at ~859 nm is evident in PANI:CSA, corresponding to π–polaron transitions associated with bipolaron formation in the highly doped state.[12,59,60]

In the PANI:CSA/70 wt.% ZnSb composite, this band intensity is suppressed and redshifted to ~881 nm, suggesting a reduction in bipolaron delocalization and the emergence of a more localized electronic structure. Similar peaks and trends of solvent traces, π–π^* transitions, polaron–π^* transition, and π–polaron transitions were seen is several studies.[12,59,60] This spectroscopic evidence aligns with XPS N 1*s* analysis, which also suggests a notable reduction in bipolaron content in the composite film. Collectively, UV–*Vis*–NIR and XPS results confirm that ZnSb incorporation significantly modulates the redox and electronic structure of PANI, shifting the equilibrium toward neutral and polaronic states while suppressing bipolaron formation and extended charge delocalization. Such evolution toward a more localized electronic structure is indicative of charge carrier confinement, a mechanism that likely contributes to the observed enhancement in Seebeck coefficient and overall thermoelectric performance while partially deteriorating the electrical conductivity.

2.4. Charge Localization Induced Tunable Thermopower and Enhanced Power Factor. In PANI:CSA/ZnSb nanocomposite films, CSA, being a bulky and flexible anion, helps uncoil the PANI backbone, enhancing planarity and π-orbital overlap between adjacent chains, particularly when processed with *m*-cresol.[19] At high enough doping (∼50% protonation), the synthesized PANI:CSA as shown in Figure 10(a), with σ ~10^2 S/cm behaves like a degenerate semiconductor or a dirty metal (i.e. σ(T) decreases with increasing temperature), suggesting presence of quasi-metallic conduction pathways having improved interchain delocalization.[19–21] Moreover, σ(T) decreases with increasing ZnSb content, suggesting interface scattering and possible disruption in the ordered regions of PANI:CSA, causing localization of charge carriers as confirmed by Raman and XPS analysis. The pristine PANI:CSA exhibits an electrical conductivity of ~148 S/cm at 323 K, which drops to 40 S/cm in PANI:CSA/70 wt% ZnSb nanocomposite films. To account for Coulomb interactions between localized charge carriers during hopping or variable-range hopping transport, the Efros–Shklovskii variable range hopping (ES-VRH) model is employed, which accounts for the formation of a soft gap in the density of states near the Fermi level.[42,61,62] The temperature-dependent carrier transport analyzed using the ES-VRH mode fits well with the temperature-dependent σ(T) as indicated in Figure 10(b).

Notably, the temperature dependence $T^{-1/2}$ exponent distinguishes ES-VRH from Mott VR and accounts for long-range Coulomb interactions between localized charge carriers, which form a soft gap in the DOS close to the Fermi level. As intercalation of ZnSb into PANI:CSA complex results in an expanded interlayer spacing, with inherent structural disorder, localization effects that may impede charge carrier mobility. The evaluated activation energy (E_a), as shown in Figure 10(c), exhibits a slight and non-monotonic increase with increasing ZnSb content. The increased charge carrier scattering from ZnSb centers and charge localization observed with higher ZnSb content results in a decreased carrier concentration (n) and carrier mobility (μ), as verified by Hall measurements near room temperature shown in Figure 10(d). In conjugated polymer systems, both energetic and spatial disorder can serve as charge-trapping centers, ultimately reducing carrier mobility.

The temperature-dependent variation of the Seebeck coefficient, S(T), for the synthesized PANI:CSA/ZnSb nanocomposite films is presented in Figure 10(e), displays a positive value of Seebeck coefficient confirming p-type behavior, characteristics of protonated PANI-based nanocomposites, rich in polarons and bipolarons, both of which are hole-like carriers. The S(T) for π conjugated polymers as validated by Watanabe et al.[62] based on Mott formula, is expressed as[61,62]

$$S \propto m^{*}T\left(\frac{1}{n}\right)^{2/3} \tag{1}$$

where m^{*}, T, and n correspond to charge carrier effective mass, temperature, and charge carrier concentration. This equation suggests that the Seebeck coefficient rises with increasing temperature or decreasing n, as observed in the synthesized polymer nanocomposites. The S(T) for all the PANI films showing inverse relation with σ(T) increases with temperature as shown in Figure 8(f), which is attributed to reduced carrier concentration and increased phonon scattering mechanisms at elevated temperatures.

With increasing contents of ZnSb nanofillers in the PANI matrix, the Seebeck coefficient is substantially increased. At 323 K, the smeared Seebeck coefficient of PANI:CSA film is typically observed to be $\leq 10\ \mu$V/K, due to their inhomogeneous polaron distribution caused local variation in carrier energy level. Thus, energetically broad and smeared DOS, often led to low and insensitive S for moderate structural or doping changes.[7] For 70 wt% ZnSb/PANI nanocomposite film, the S was increased to ≈ 50 μV/K (~ 6 times) at 323 K and up to ~ 60 μV/K at 373 K. The higher value of the S corresponds to lowering n as shown by Hall measurement, reduction in bipolarons level that may lead to charge localization as suggested by Raman, XPS, and UV-vis NIR analysis.[41,56–58] By introducing localized states or affecting the band structure, ZnSb may induce an asymmetric DOS near the Fermi level,[64] also implied by altered and distorted structure hybridized PANI:CSA/ZnSb nanocomposite films and XPS spectra. Such asymmetry favors higher S, as it depends on the difference in the average energy of electrons above and below the Fermi level. Thus, existence of both partially delocalized and localized states, introduced via ZnSb intercalation, leads to a combined effect of reduced σ and an increased S, wherein the partial delocalization probably comes from existing singly charged polarons levels as seen from XPS study, and the partial localization states probably arise from suppressed bipolarons level significantly.

Figure 11(a) shows a plot of electrical conductivity versus Seebeck coefficient for reported PANI-based nanocomposites with our reported σ vs. S values, showing inverse correlation and a largely low values of S attained for polymer nanocomposites. Figure 11(b) demonstrates an inverse and varying relationship between S(T) and σ(T) with varying ZnSb content and temperature (373 – 293 K) from right to left, suggestive of weak localization and non-degenerate transport regime.[61,62] As a semi-conductive filler, the distribution, morphology, and interfacial phenomena of intercalated ZnSb nanoparticles within polymeric PANI:CSA matrix promote charge localization, while for high protonation level i.e. polarons and bipolarons in PANI:CSA complex promotes delocalization.[41] Figure 11(c) shows the PF of the PANI:CSA and PANI:CSA/ZnSb nanocomposite films. The value of the power factor can be calculated from a simple expression (PF = $S^2\sigma$). A higher PF ~ 10 μW/m.K^2 at 333 K is calculated for 70 wt% ZnSb/PANI nanocomposite film, 10 times larger than the pristine PANI:CSA film (PF ~ 1

μW/m.K^2), thus highlighting the prospect of structurally compatible semiconducting fillers for improving and tuning the S effectively. To assess the impact of oxidative and humid exposure, electrical measurements after ~2 months showed slight reductions in conductivity and Seebeck coefficient, likely due to PANI chain degradation (Figure S13, Supplementary Section S6).

Further enhancement of the power factor may be achieved by increasing charge carrier mobility through the incorporation of surface-functionalized carbon nanotubes (CNTs) or graphene or structural reordering via post-synthesis treatments that enhance backbone planarity and conjugation length, thereby promoting long-range charge transport. Figure 11(d) compares various studies, highlighting that while most have focused on Tellurium (Te)-based fillers, herein we employ a widely recognized, non-toxic, Te-free material ZnSb nanofillers blending in PANI:CSA to achieve power factor optimization. Additionally, co-doping and hybridization with metal oxides (e.g., TiO_2, Fe_2O_3, CuO), 2D materials (such as MoS_2, WS_2, and MXenes), represent a promising direction for future development of PANI based nanocomposite films for thermoelectric applications.

2.5. Fabrication of Flexible Thermoelectric Generator (FTEG). To assess the practical applicability of the optimized PANI:CSA/70 wt.% ZnSb nanocomposite, a flexible device constituting patterned composite legs (~ 15×5 mm^2 each) on a Kapton (polyimide) substrate. As shown in Figure 12(a), the legs were connected in series with silver contacts, and copper wires were attached using silver paste to ensure good ohmic contact. The device was tested under two conditions: (i) body heat harvesting, where it was attached to a human forearm using Kapton tape, generating an output voltage (V_{OC}) ~ 0.9 mV from a ~10 K skin-to-air temperature gradient (ΔT) (Figure 12b); and (ii) hot plate heating, where it produced up to ~6.7 mV at a ~50 K gradient (Figure 12c), consistent with the reported values.[26,28,55,56] The device retained its flexibility and stable performance during attachment to curved surfaces, demonstrating its robustness and feasibility for wearable electronics demanding body-conformable adaptability.

3. **Conclusion.** We report flexible, free-standing PANI:CSA and PANI:CSA/ZnSb nanocomposite films via solution drop-casting, with intercalation of ZnSb nanofillers attained in *m*-cresol medium. Lattice expansion and reoriented chain conformation with a marginal variation in unit cell parameters, was evaluated for pseudo-orthorhombic PANI:CSA complex upon orthorhombic ZnSb nanofillers intercalation, which disrupts original ordering and led to emergence of new crystalline domains. Raman spectra confirm conformational changes and charge localization in the polymer matrix, while XPS and UV-Vis-NIR analyses indicate a transition from bipolaronic to polaronic states, accompanied by changes in oxidation state and doping levels, consistent with Hall measurement results. These findings suggest that incorporating semiconducting fillers like ZnSb into conducting polymers modulates charge transport by suppressing bipolaron formation and increasing carrier scattering and localization, leading to an improved Seebeck coefficient (≈ 50 μV/K) and power factor (≈ 10 $\mu W/m\cdot K^2$) at room temperature for higher ZnSb content. A flexible thermoelectric generator (FTEG) fabricated with six PANI:CSA/70 wt.% ZnSb nanocomposite films generated ~0.9 mV on a human wrist, and ~6.7 mV under a 50 K temperature gradient, showcasing its possible practical potential. Thus, semiconducting nanofillers induced charge localization presents a promising strategy for tuning the Seebeck coefficient and enhancing the power factor, thereby enabling the development of flexible TE films suited for wearable electronics and body heat recovery, especially where mechanical flexibility and environmental compatibility are essential

Associated Content.

Supporting Information. Details of experimental procedures for ZnSb synthesis, PANI:CSA/ZnSb hybrid film fabrication, and characterization methods. Additional data include structural parameters, crystallographic analysis, SEM images, key Raman intensity ratios with interpretations, bending test results, XPS survey spectra, and aging stability assessments.

Acknowledgment. This work was supported by the JST Mirai Program, Japan, Grant Number JPMJMI19A1. A.S. gratefully acknowledges financial support from JST, the establishment of university fellowships towards the creation of science technology innovation, Grant Number JPMJFS 2106.

Conflict of Interest: There is no conflict of interest to declare.

Data availability statement: The data that supports the findings of this study are available upon request from the authors.

TABLES

Table 1. (*hkl*) indexation based on pseudo-orthorhombic lattice symmetry (Space group: Pc2a, 32) of PANI:CSA complex in emeraldine salt proposed by Pouget et al.[50] and evaluated *d* Spacing of synthesized PANI:CSA/ZnSb nanocomposite films.

(*hkl*)	**Pouget et al.[50]**	**This Work**					
		PANI:CSA	**PANI : CSA/ZnSb Nanocomposite Films**				
			30%	**40%**	**50%**	**60%**	**70%**
(010)	7.88	7.85	-	-	-	-	-
(101)	5.87	5.95	8.79	8.80	8.74	8.84	8.83
(002)	-	5.40	7.51	7.51	7.48	7.41	7.42
(111)	-	4.93	6.54	6.53	6.51	6.56	6.54
(012)	4.38	4.61	5.92	5.92	5.91	5.86	5.86
(102)	4.18	4.43	5.68	5.68	5.66	5.67	5.67
(020)	-	4.27	5.21	5.20	5.19	5.19	5.17
(112)	-	3.97	4.86	4.86	4.85	4.85	4.85
(200)	3.57	3.76	4.61	4.60	4.59	4.68	4.67
(201)	-	3.57	4.32	4.31	4.30	4.37	4.37
(121)	-	3.56	4.17	4.16	4.16	4.16	4.15
(210)	3.24	3.45	4.13	4.12	4.11	4.17	4.16
(022)	-	3.44	3.98	3.98	3.98	3.96	3.94

FIGURES

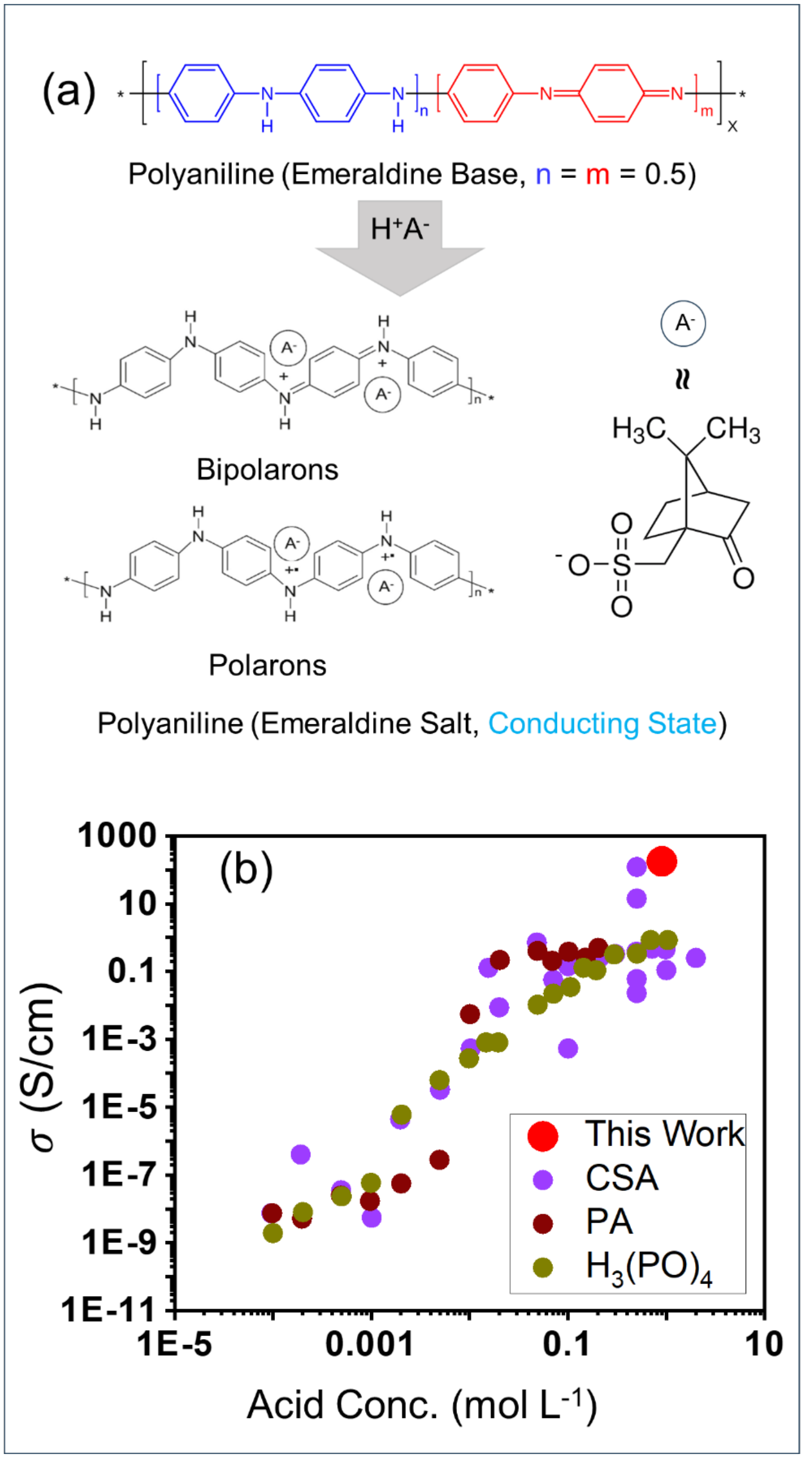

Figure 1. **(a)** Generic structure of emeraldine base form of polyaniline, which transforms to emeraldine salt form, constituting polarons and bipolarons. **(b)** Dependence of electrical conductivity vs. protic acid concentration.[24–27]

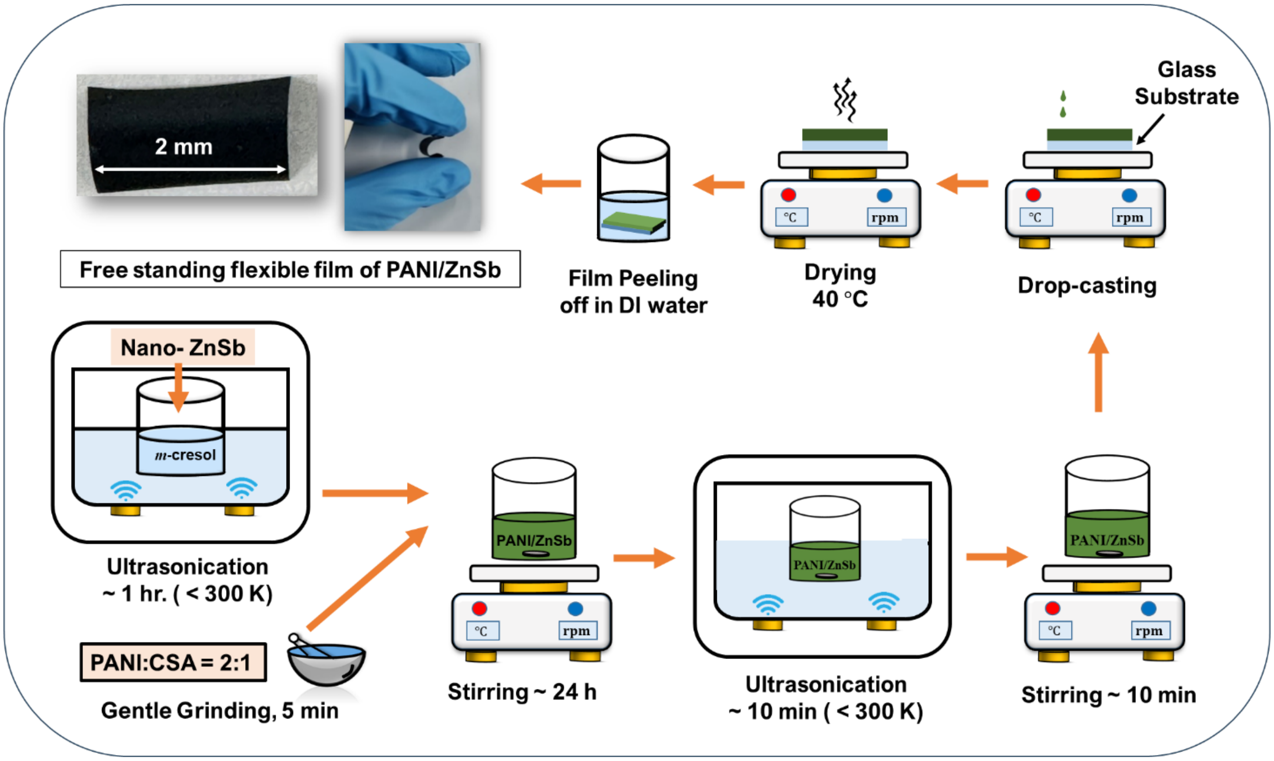

Figure 2. Schematic representing fabrication process of flexible PANI:CSA/ZnSb nanocomposite free-standing film.

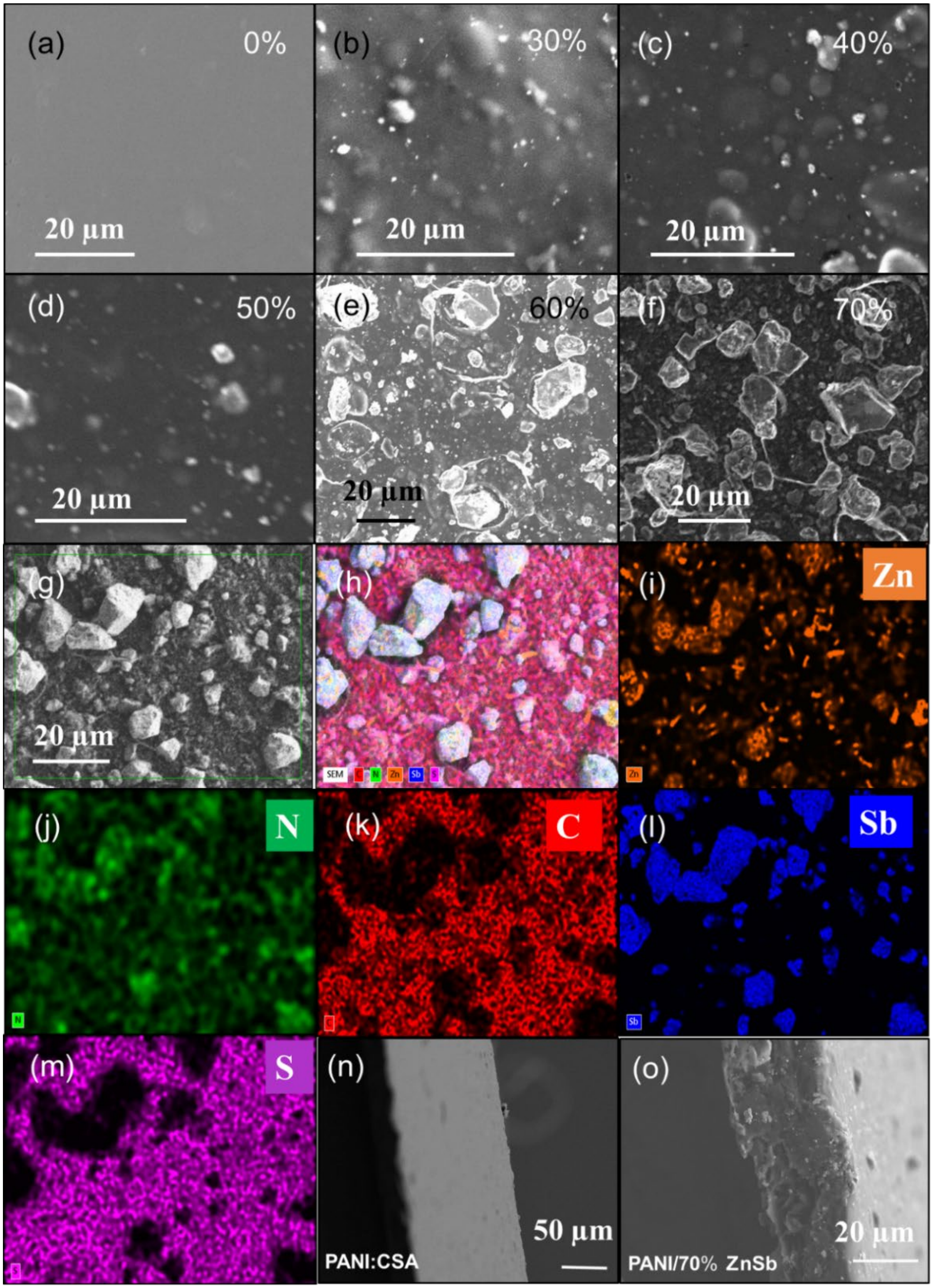

Figure 3. (*a – f*) SEM micrographs illustrating the granular morphology of ZnSb clusters with increasing ZnSb content. (*g – m*) EDX elemental mapping of the marked region highlights the distinct distribution of ZnSb clusters within the polymeric PANI matrix. (*n – o*) SEM image of cross-section of PANI:CSA & PANI:CSA/70 wt.% ZnSb nanocomposite film, respectively.

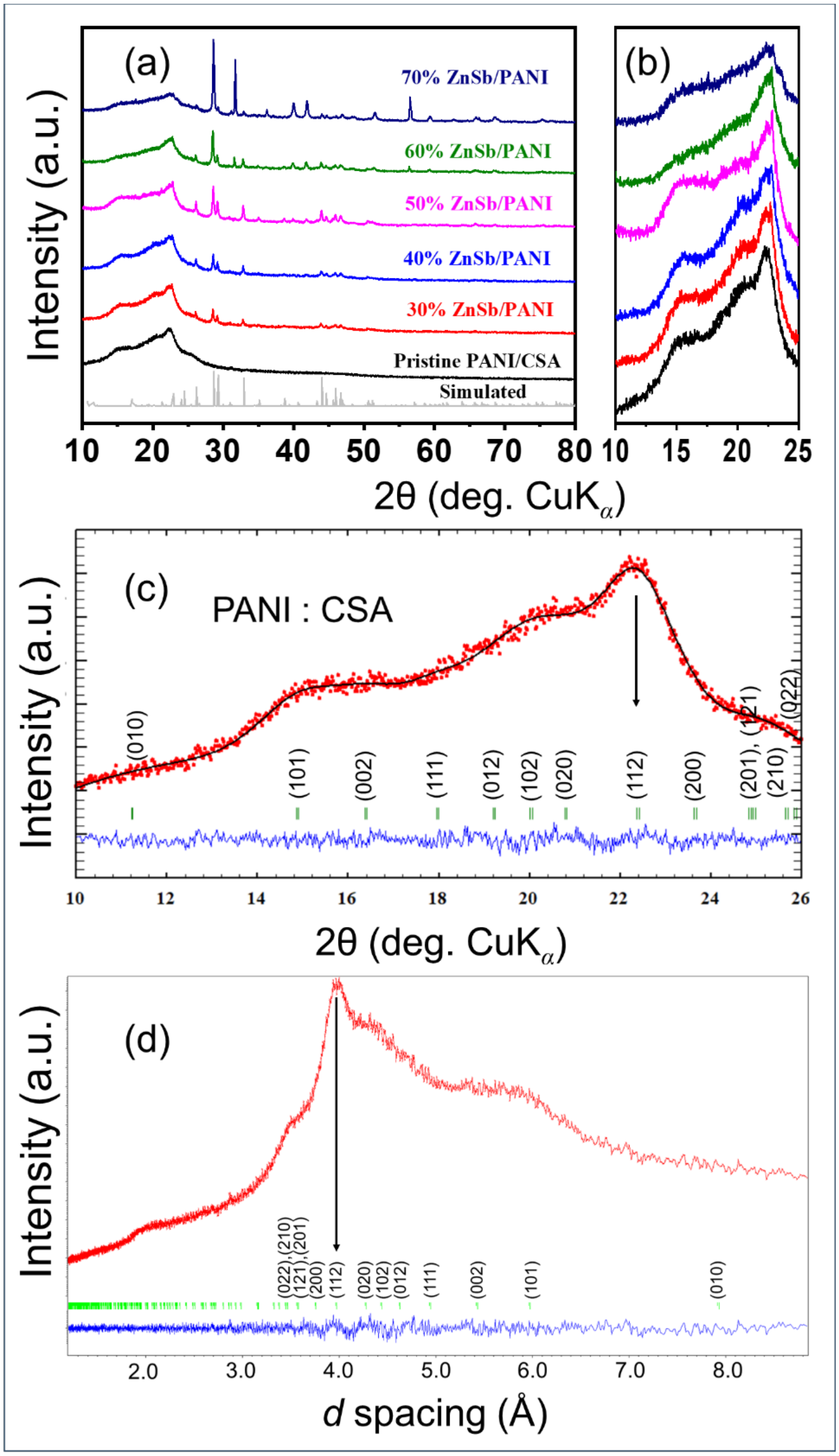

Figure 4. (a) X-Ray diffraction patterns of pristine PANI:CSA, and PANI:CSA/ZnSb (30 – 70 wt.%) nanocomposite films, (b) Characteristic reflection corresponding to PANI:CSA complex shown in a magnified range, (c) Le Bail refined structure implying pseudo-orthorhombic symmetry (Pc2a, 32), with corresponding (d) *d*-spacing for unfilled PANI:CSA complex.

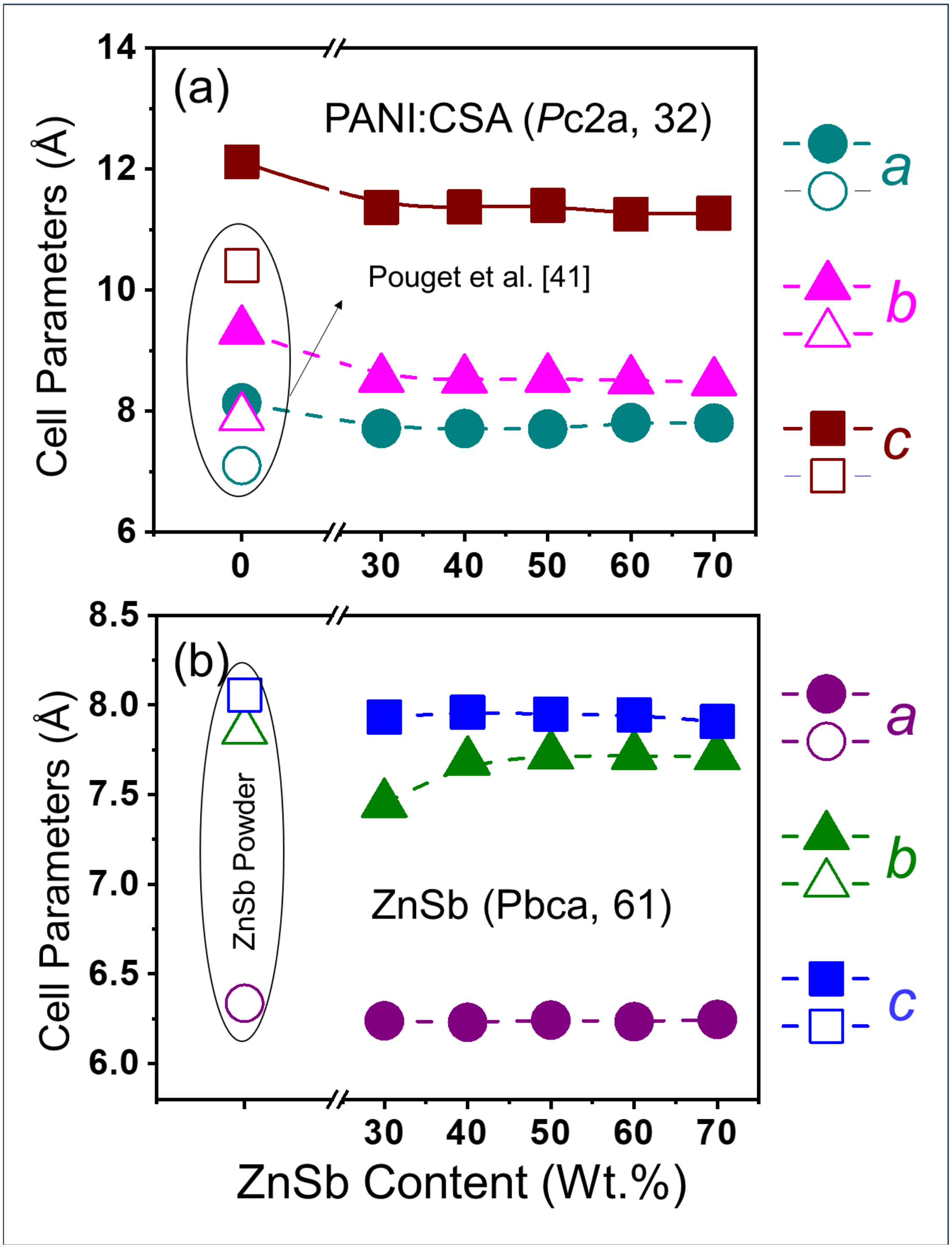

Figure 5. Refined lattice parameter for pseudo-orthorhombic (a) PANI:CSA Complex with empty symbols corresponding to values evaluated by Pouget et al.[50] (b) Orthorhombic ZnSb phase in PANI:CSA/ZnSb nanocomposite vs. ZnSb content.

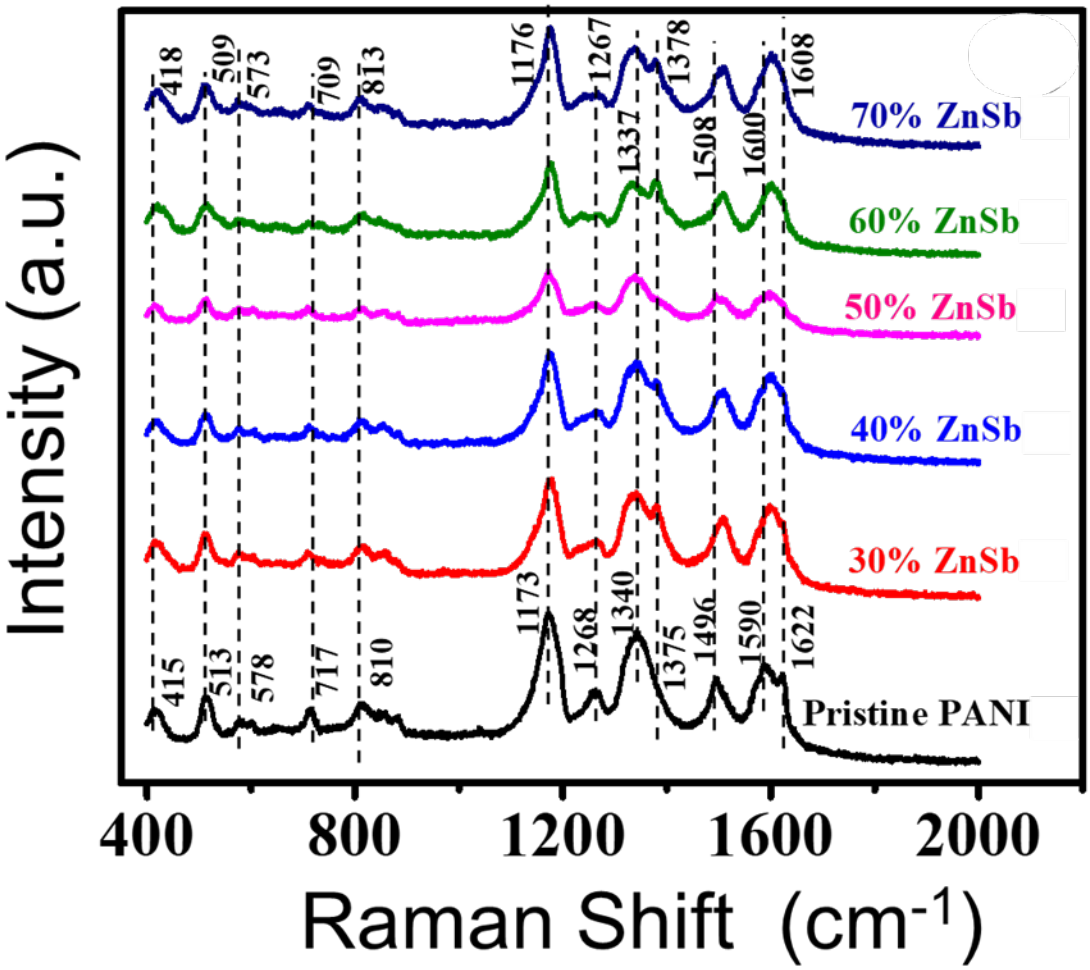

Figure 6. Raman spectra of the PANI:CSA, and PANI:CSA/ZnSb (30 – 70 wt. %) nanocomposite films.

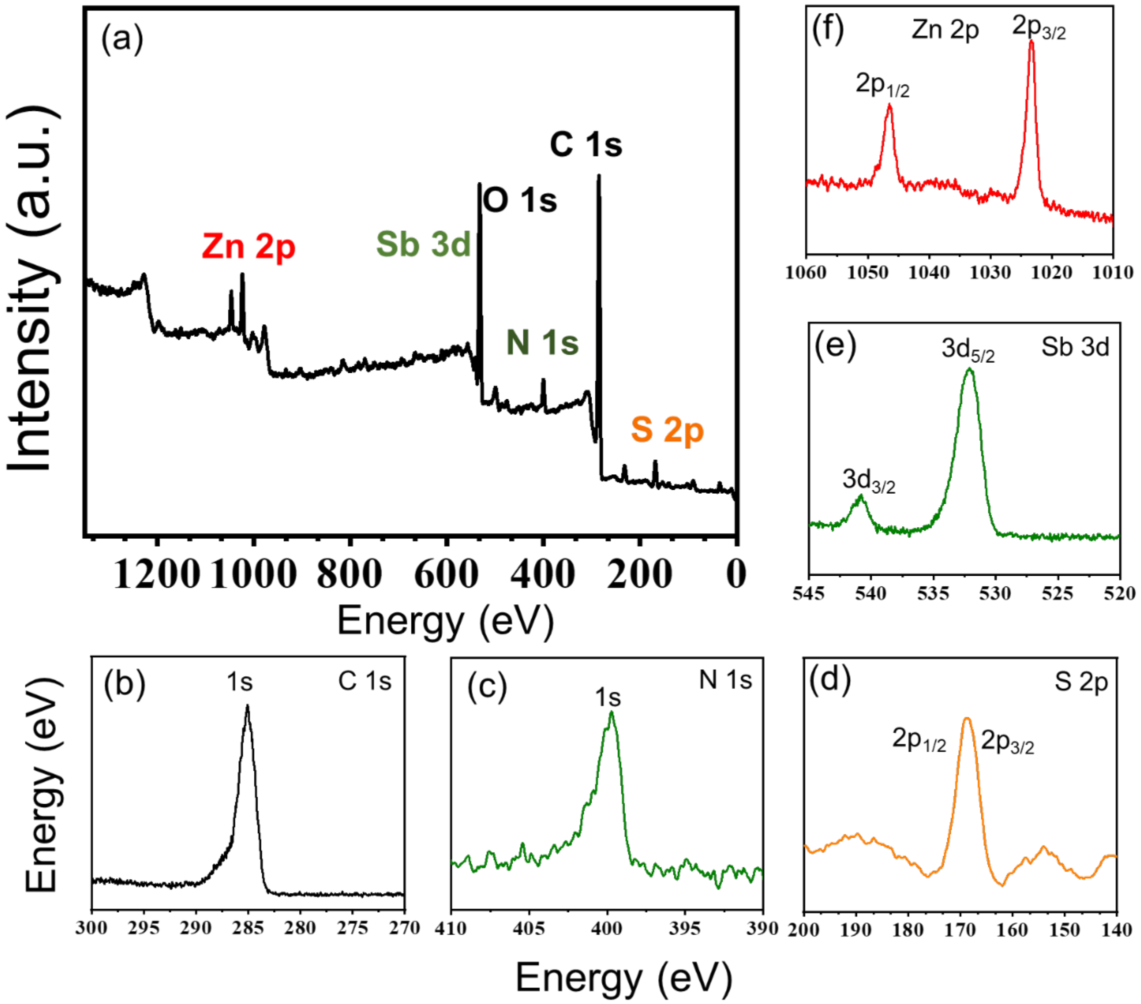

Figure 7. (a) XPS survey spectra; (b) –(f) high resolution peaks of C 1s, N 1*s*, S 2*p*, Sb 3*d*, and Zn 2*p*, respectively, of the :PANI:CSA/70 wt.% ZnSb nanocomposite film.

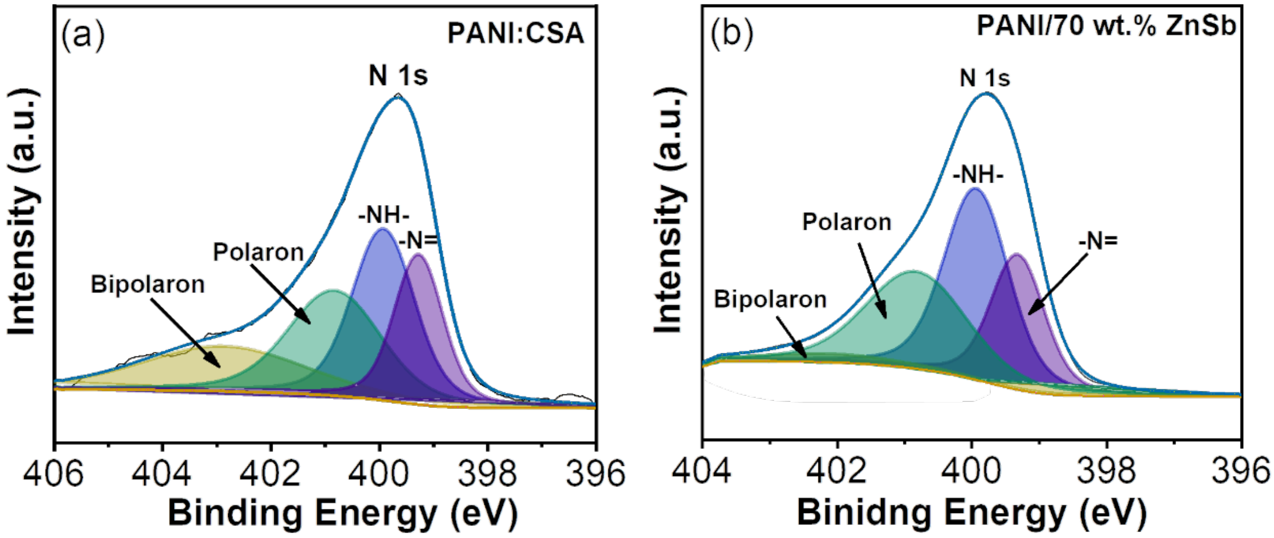

Figure 8. Deconvoluted N 1s XPS spectral peaks for (a) PANI:CSA, & (b) PANI:CSA/70 wt.% ZnSb nanocomposite film

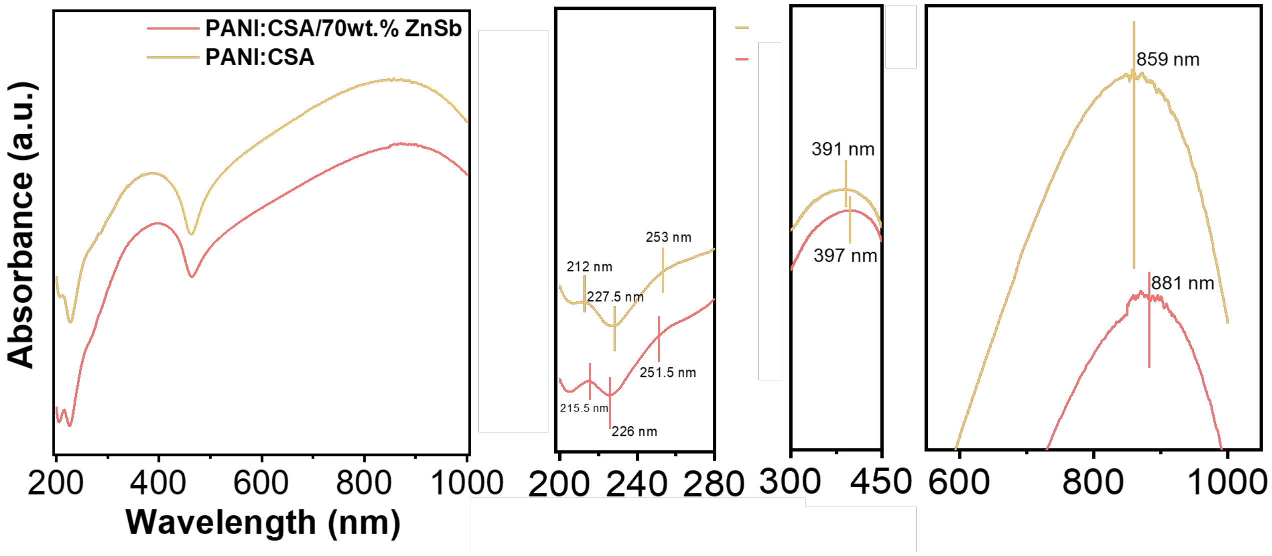

Figure 9. UV–Vis–NIR absorption spectra analysis of PANI:CSA and PANI:CSA/70 wt.% ZnSb composite films.

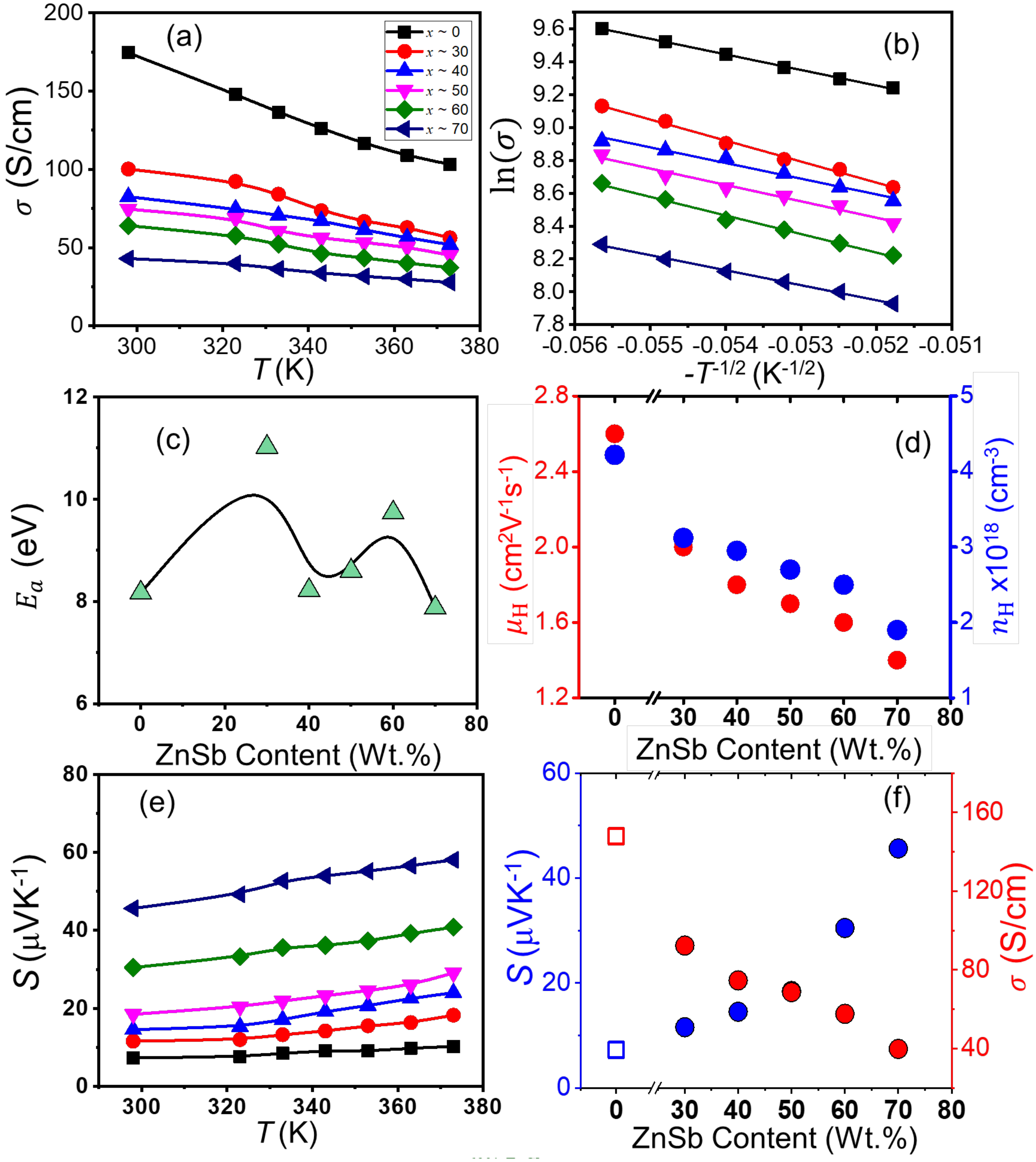

Figure 10. Temperature dependence of (a) electrical conductivity, (b) ES-VRH model fitting with a temperature exponent of 1/2 demonstrating linear behavior, (c) activation energy derived for variable-range hopping conduction, (d) carrier concentration and mobility as a function of ZnSb content from room-temperature Hall measurements, (e) Seebeck coefficient variation with temperature, and (f) the inverse relationship between the Seebeck coefficient and electrical conductivity for PANI:CSA and ZnSb-incorporated PANI:CSA nanocomposite flexible films at varying ZnSb Weight percentages.

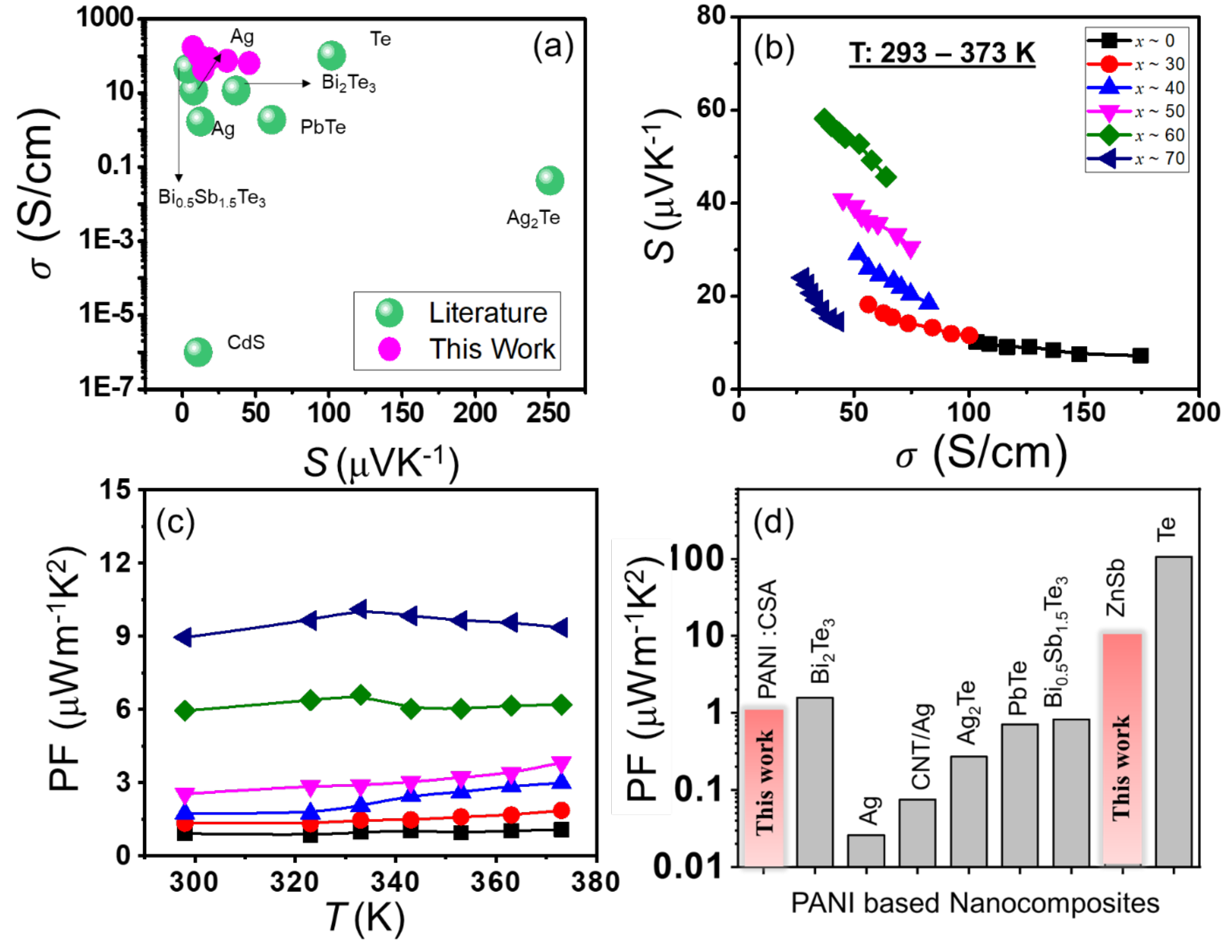

Figure 11. (a) Electrical conductivity as a function of the Seebeck coefficient for reported PANI-based nanocomposites[28–35]; (b) Jonker plot illustrating the relationship between Seebeck coefficient and electrical conductivity; (c) Temperature-dependent power factor of PANI-based materials; and (d) Comparison of reported power factor values for PANI-based nanocomposites[28–34].

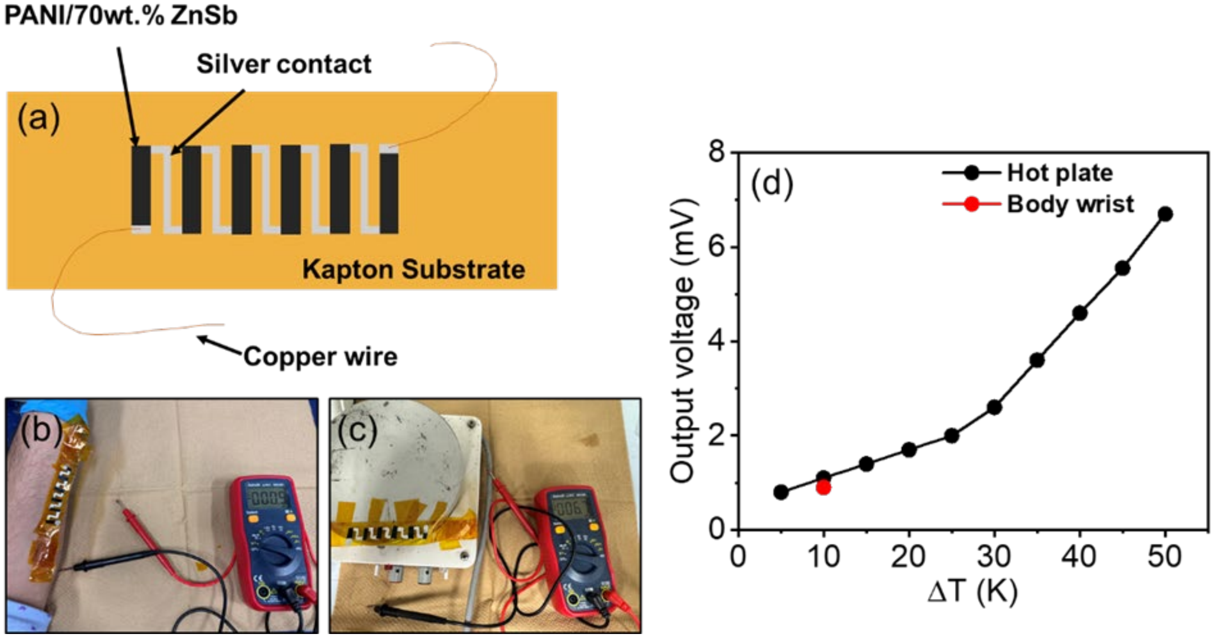

Figure 12. Flexible thermoelectric device based on PANI:CSA/70 wt.% ZnSb: (a) Device schematic on Kapton substrate with alternating PANI:CSA/70 wt.% ZnSb nanocomposite flexible films; (b) On-body demonstration under body heat; (c) Output under hot plate-induced ΔT; (d) Output voltage (V_o) vs. ΔT confirming thermoelectric response.

References

[1] S. Xu, X.-L. Shi, M. Dargusch, C. Di, J. Zou, Z.-G. Chen, Conducting polymer-based flexible thermoelectric materials and devices: From mechanisms to applications, Progress in Materials Science 121 (2021) 100840. https://doi.org/10.1016/j.pmatsci.2021.100840.

[2] T. Mori, S. Priya, Materials for energy harvesting: At the forefront of a new wave, MRS Bull. 43 (2018) 176–180. https://doi.org/10.1557/mrs.2018.32.

[3] G. Prunet, F. Pawula, G. Fleury, E. Cloutet, A.J. Robinson, G. Hadziioannou, A. Pakdel, A review on conductive polymers and their hybrids for flexible and wearable thermoelectric applications, Materials Today Physics 18 (2021) 100402. https://doi.org/10.1016/j.mtphys.2021.100402.

[4] M. Bharti, A. Singh, S. Samanta, D.K. Aswal, Conductive polymers for thermoelectric power generation, Progress in Materials Science 93 (2018) 270–310. https://doi.org/10.1016/j.pmatsci.2017.09.004.

[5] I. Petsagkourakis, K. Tybrandt, X. Crispin, I. Ohkubo, N. Satoh, T. Mori, Thermoelectric materials and applications for energy harvesting power generation, Science and Technology of Advanced Materials 19 (2018) 836–862. https://doi.org/10.1080/14686996.2018.1530938.

[6] Z. Zhang, Z. Wei, M. Wan, Nanostructures of Polyaniline Doped with Inorganic Acids, Macromolecules 35 (2002) 5937–5942. https://doi.org/10.1021/ma020199v.

[7] M. Pope, C.E. Swenberg, Electronic Processes in Organic Crystals and Polymers, Second Edition, Oxford University PressNew York, NY, 1999. https://doi.org/10.1093/oso/9780195129632.001.0001.

[8] N. Nandihalli, C.-J. Liu, T. Mori, Polymer based thermoelectric nanocomposite materials and devices: Fabrication and characteristics, Nano Energy 78 (2020) 105186. https://doi.org/10.1016/j.nanoen.2020.105186.

[9] Y. Wang, H. Pang, Q. Guo, N. Tsujii, T. Baba, T. Baba, T. Mori, Flexible *n* -Type Abundant Chalcopyrite/PEDOT:PSS/Graphene Hybrid Film for Thermoelectric Device Utilizing Low-Grade Heat, ACS Appl. Mater. Interfaces 13 (2021) 51245–51254. https://doi.org/10.1021/acsami.1c15232.

[10] Y. Wang, R. Chetty, Z. Liu, L. Wang, T. Ohsawa, W. Gao, T. Mori, A facile route to fabricating a crack-free $Mg_{0.99} Cu_{0.01} Ag_{0.97} Sb_{0.99}$ /graphene/PEDOT:PSS thermoelectric film on a flexible substrate, J. Mater. Chem. C 10 (2022) 12610–12620. https://doi.org/10.1039/D2TC02176E.

[11] A.K. Yadav, N. Mohammad, E. Chamanehpour, Y.K. Mishra, P.K. Khanna, Polyaniline (PANI) nanocomposites with Se, Te and their metal chalcogenides: a review, RSC Appl. Polym. 2 (2024) 775–794. https://doi.org/10.1039/D4LP00093E.

[12] H. Li, Y. Liang, Y. Liu, S. Liu, P. Li, C. He, Engineering doping level for enhanced thermoelectric performance of carbon nanotubes/polyaniline composites, Composites Science and Technology 210 (2021) 108797. https://doi.org/10.1016/j.compscitech.2021.108797.

[13] A.G. Macdiarmid, J.-C. Chiang, M. Halpern, W.-S. Huang, S.-L. Mu, L.D. Nanaxakkara, S.W. Wu, S.I. Yaniger, “Polyaniline”: Interconversion of Metallic and Insulating Forms, Molecular Crystals and Liquid Crystals 121 (1985) 173–180. https://doi.org/10.1080/00268948508074857.

[14] P. Kaushik, R. Bharti, R. Sharma, M. Verma, R.T. Olsson, A. Pandey, Progress in synthesis and applications of Polyaniline-Coated Nanocomposites: A comprehensive review, European Polymer Journal 221 (2024) 113574. https://doi.org/10.1016/j.eurpolymj.2024.113574.

[15] G.-R. Li, Z.-P. Feng, J.-H. Zhong, Z.-L. Wang, Y.-X. Tong, Electrochemical Synthesis of Polyaniline Nanobelts with Predominant Electrochemical Performances, Macromolecules 43 (2010) 2178–2183. https://doi.org/10.1021/ma902317k.

[16] J. Scotto, M.I. Florit, D. Posadas, About the species formed during the electrochemical half oxidation of polyaniline: Polaron-bipolaron equilibrium, Electrochimica Acta 268 (2018) 187–194. https://doi.org/10.1016/j.electacta.2018.02.066.

[17] R. Djara, Y. Holade, A. Merzouki, N. Masquelez, D. Cot, B. Rebiere, E. Petit, P. Huguet, C. Canaff, S. Morisset, T.W. Napporn, D. Cornu, S. Tingry, Insights from the Physicochemical and Electrochemical Screening of the Potentiality of the Chemically Synthesized Polyaniline, J. Electrochem. Soc. 167 (2020) 066503. https://doi.org/10.1149/1945-7111/ab7d40.

[18] N. Sirotkin, A. Khlyustova, Plasma Synthesis and Characterization of PANI + WO3 Nanocomposites and their Supercapacitor Applications, J. Compos. Sci. 7 (2023) 174. https://doi.org/10.3390/jcs7040174.

[19] Q. Yao, Q. Wang, L. Wang, Y. Wang, J. Sun, H. Zeng, Z. Jin, X. Huang, L. Chen, The synergic regulation of conductivity and Seebeck coefficient in pure polyaniline by chemically changing the ordered degree of molecular chains, J. Mater. Chem. A 2 (2014) 2634–2640. https://doi.org/10.1039/C3TA14008C.

[20] A.B. Kaiser, Systematic Conductivity Behavior in Conducting Polymers: Effects of Heterogeneous Disorder, Adv. Mater. 13 (2001) 927–941. https://doi.org/10.1002/1521-4095(200107)13:12/13<927::AID-ADMA927>3.0.CO;2-B.

[21] A.B. Kaiser, V. Skákalová, Electronic conduction in polymers, carbon nanotubes and graphene, Chem. Soc. Rev. 40 (2011) 3786. https://doi.org/10.1039/c0cs00103a.

[22] S. Sinha, S. Bhadra, D. Khastgir, Effect of dopant type on the properties of polyaniline, J of Applied Polymer Sci 112 (2009) 3135–3140. https://doi.org/10.1002/app.29708.

[23] H. Yan, T. Ohta, N. Toshima, Stretched Polyaniline Films Doped by (±)-10-Camphorsulfonic Acid: Anisotropy and Improvement of Thermoelectric Properties, Macromol. Mater. Eng. 286 (2001) 139–142. https://doi.org/10.1002/1439-2054(20010301)286:3<139::AID-MAME139>3.0.CO;2-F.

[24] C. Nath, A. Kumar, Y.-K. Kuo, G.S. Okram, High thermoelectric figure of merit in nanocrystalline polyaniline at low temperatures, Applied Physics Letters 105 (2014) 133108. https://doi.org/10.1063/1.4897146.

[25] M. Singh, A.K. Gautam, M. Faraz, N. Khare, Thermoelectric performance of (±) Camphor-10-sulfonic acid doped polyaniline/graphitic carbon nitride composite films, Eur. Phys. J. Plus 137 (2022) 1251. https://doi.org/10.1140/epjp/s13360-022-03451-7.

[26] M. Singh, A.K. Gautam, M. Faraz, N. Khare, Flexible, Freestanding Ternary Nanocomposite Thick Film of Polyaniline/WS_2 /CNTs for Efficient Thermoelectric Application, ACS Appl. Energy Mater. 7 (2024) 133–144. https://doi.org/10.1021/acsaem.3c02331.

[27] D. Geethalakshmi, N. Muthukumarasamy, R. Balasundaraprabhu, CSA-doped PANI semiconductor nanofilms: synthesis and characterization, J Mater Sci: Mater Electron 26 (2015) 7797–7803. https://doi.org/10.1007/s10854-015-3427-z.

[28] Y. Wang, S.M. Zhang, Y. Deng, Flexible low-grade energy utilization devices based on high-performance thermoelectric polyaniline/tellurium nanorod hybrid films, J. Mater. Chem. A 4 (2016) 3554–3559. https://doi.org/10.1039/C6TA01140C.

[29] Y.Y. Wang, K.F. Cai, J.L. Yin, B.J. An, Y. Du, X. Yao, In situ fabrication and thermoelectric properties of PbTe–polyaniline composite nanostructures, J Nanopart Res 13 (2011) 533–539. https://doi.org/10.1007/s11051-010-0043-y.

[30] K. Chatterjee, M. Mitra, K. Kargupta, S. Ganguly, D. Banerjee, Synthesis, characterization and enhanced thermoelectric performance of structurally ordered cable-like novel

polyaniline–bismuth telluride nanocomposite, Nanotechnology 24 (2013) 215703. https://doi.org/10.1088/0957-4484/24/21/215703.

[31] C. Guo, F. Chu, P. Chen, J. Zhu, H. Wang, L. Wang, Y. Fan, W. Jiang, Effectively enhanced thermopower in polyaniline/Bi0.5Sb1.5Te3 nanoplate composites via carrier energy scattering, J Mater Sci 53 (2018) 6752–6762. https://doi.org/10.1007/s10853-017-1958-9.

[32] W. Wang, S. Sun, S. Gu, H. Shen, Q. Zhang, J. Zhu, L. Wang, W. Jiang, One-pot fabrication and thermoelectric properties of Ag nanoparticles–polyaniline hybrid nanocomposites, RSC Adv. 4 (2014) 26810–26816. https://doi.org/10.1039/C4RA02136C.

[33] F. Roussel, R. Chen Yu King, M. Kuriakose, M. Depriester, A. Hadj-Sahraoui, C. Gors, A. Addad, J.-F. Brun, Electrical and thermal transport properties of polyaniline/silver composites and their use as thermoelectric materials, Synthetic Metals 199 (2015) 196–204. https://doi.org/10.1016/j.synthmet.2014.11.020.

[34] Y.Y. Wang, K.F. Cai, J.L. Yin, Y. Du, X. Yao, One-pot fabrication and thermoelectric properties of Ag2Te–polyaniline core–shell nanostructures, Materials Chemistry and Physics 133 (2012) 808–812. https://doi.org/10.1016/j.matchemphys.2012.01.098.

[35] P.V. More, C. Hiragond, A. Dey, P.K. Khanna, Band engineered p-type RGO–CdS–PANI ternary nanocomposites for thermoelectric applications, Sustainable Energy Fuels 1 (2017) 1766–1773. https://doi.org/10.1039/C7SE00290D.

[36] M. Mitra, C. Kulsi, K. Kargupta, S. Ganguly, D. Banerjee, Composite of polyaniline-bismuth selenide with enhanced thermoelectric performance, J of Applied Polymer Sci 135 (2018) 46887. https://doi.org/10.1002/app.46887.

[37] H. Ju, D. Park, J. Kim, Fabrication of Polyaniline-Coated SnSeS Nanosheet/Polyvinylidene Difluoride Composites by a Solution-Based Process and Optimization for Flexible Thermoelectrics, ACS Appl. Mater. Interfaces 10 (2018) 11920–11925. https://doi.org/10.1021/acsami.7b19667.

[38] W. W. Focke, G. E. Wnek, Conduction mechanisms in polyaniline (emeraldine salt), Journal of Electroanalytical Chemistry and Interfacial Electrochemistry 256 (1988) 343–352. https://doi.org/10.1016/0022-0728(88)87008-6.

[39] G. Tzamalis, N.A. Zaidi, C.C. Homes, A.P. Monkman, Doping-dependent studies of the Anderson-Mott localization in polyaniline at the metal-insulator boundary, Phys. Rev. B 66 (2002) 085202. https://doi.org/10.1103/PhysRevB.66.085202.

[40] K. Lee, S. Cho, S. Heum Park, A.J. Heeger, C.-W. Lee, S.-H. Lee, Metallic transport in polyaniline, Nature 441 (2006) 65–68. https://doi.org/10.1038/nature04705.

[41] N.J. Pinto, P.K. Kahol, B.J. McCormick, N.S. Dalal, H. Wan, Charge transport and electron localization in polyaniline derivatives, Phys. Rev. B 49 (1994) 13983–13986. https://doi.org/10.1103/PhysRevB.49.13983.

[42] A.L. Efros, M. Pollak, Electron-Electron Interactions in Disordered Systems, in: March 1, De Gruyter, 1986: pp. 497–498. https://doi.org/10.1515/9783112494721-070.

[43] S. Shekhar, V. Prasad, S.V. Subramanyam, Anomalous Efros–Shklovskii variable range hopping conduction in composites of polymer and iron carbide nanoparticles embedded in carbon, Physics Letters A 360 (2006) 390–393. https://doi.org/10.1016/j.physleta.2006.08.043.

[44] L.W. Shacklette, Dipole and hydrogen-bonding interactions in polyaniline: a mechanism for conductivity enhancement, Synthetic Metals 65 (1994) 123–130. https://doi.org/10.1016/0379-6779(94)90173-2.

[45] K.-H. Lee, B.J. Park, D.H. Song, I.-J. Chin, H.J. Choi, The role of acidic m-cresol in polyaniline doped by camphorsulfonic acid, Polymer 50 (2009) 4372–4377. https://doi.org/10.1016/j.polymer.2009.07.009.

[46] P. Sekar, B. Anothumakkool, S. Kurungot, 3D Polyaniline Porous Layer Anchored Pillared Graphene Sheets: Enhanced Interface Joined with High Conductivity for Better Charge Storage Applications, ACS Appl. Mater. Interfaces 7 (2015) 7661–7669. https://doi.org/10.1021/acsami.5b00504.

[47] C. Yang, L. Zhang, N. Hu, Z. Yang, Y. Su, S. Xu, M. Li, L. Yao, M. Hong, Y. Zhang, Rational design of sandwiched polyaniline nanotube/layered graphene/polyaniline nanotube papers for high-volumetric supercapacitors, Chemical Engineering Journal 309 (2017) 89–97. https://doi.org/10.1016/j.cej.2016.09.115.

[48] E.A. Sanches, A.D.S. Carolino, A.L.D. Santos, E.G.R. Fernandes, D.M. Trichês, Y.P. Mascarenhas, The Use of Le Bail Method to Analyze the Semicrystalline Pattern of a Nanocomposite Based on Polyaniline Emeraldine-Salt Form and α -Al_2 O_3, Advances in Materials Science and Engineering 2015 (2015) 1–8. https://doi.org/10.1155/2015/375312.

[49] D. Djurado, Y.F. Nicolau, I. Dalsegg, E.J. Samuelsen, X-ray scattering study of CSA protonated polyaniline films and powders, Synthetic Metals 84 (1997) 121–122. https://doi.org/10.1016/S0379-6779(97)80675-3.

[50] J.P. Pouget, M.E. Jozefowicz, A.J. Epstein, X. Tang, A.G. MacDiarmid, X-ray structure of polyaniline, Macromolecules 24 (1991) 779–789. https://doi.org/10.1021/ma00003a022.

[51] T.B.E. Grønbech, H. Kasai, J. Zhang, E. Nishibori, B.B. Iversen, Weak Bonding and Anharmonicity in Thermoelectric ZnSb, Adv Funct Materials 34 (2024) 2401703. https://doi.org/10.1002/adfm.202401703.

[52] V. Petkov, V. Parvanov, P. Trikalitis, C. Malliakas, T. Vogt, M.G. Kanatzidis, Three-Dimensional Structure of Nanocomposites from Atomic Pair Distribution Function Analysis: Study of Polyaniline and (Polyaniline)$_{0.5}$ V_2 O_5 ·1.0H_2 O, J. Am. Chem. Soc. 127 (2005) 8805–8812. https://doi.org/10.1021/ja051315n.

[53] S.A. Ture, V.B. Patil, C.V. Yelamaggad, R. Martínez-Máñez, V. Abbaraju, Understanding of mechanistic perspective in sensing of energetic nitro compounds through spectroscopic and electrochemical studies, J of Applied Polymer Sci 138 (2021) 50776. https://doi.org/10.1002/app.50776.

[54] Z. Morávková, P. Bober, Writing in a Polyaniline Film with Laser Beam and Stability of the Record: A Raman Spectroscopy Study, International Journal of Polymer Science 2018 (2018) 1–8. https://doi.org/10.1155/2018/1797216.

[55] D. Ji, B. Li, B.T. Raj, X. Li, D. Zhang, M. Rezeq, W. Cantwell, L. Zheng, In Situ Surface Polymerization of PANI/SWCNT Bilayer Film: Effective Composite for Improving Seebeck Coefficient and Power Factor, Adv Materials Inter 12 (2025) 2400566. https://doi.org/10.1002/admi.202400566.

[56] L. Wang, Q. Yao, W. Shi, S. Qu, L. Chen, Engineering carrier scattering at the interfaces in polyaniline based nanocomposites for high thermoelectric performances, Mater. Chem. Front. 1 (2017) 741–748. https://doi.org/10.1039/C6QM00188B.

[57] X. Guan, J. Ouyang, Enhancement of the Seebeck Coefficient of Organic Thermoelectric Materials via Energy Filtering of Charge Carriers, CCS Chem 3 (2021) 2415–2427. https://doi.org/10.31635/ccschem.021.202101069.

[58] S.A. Gregory, R. Hanus, A. Atassi, J.M. Rinehart, J.P. Wooding, A.K. Menon, M.D. Losego, G.J. Snyder, S.K. Yee, Quantifying charge carrier localization in chemically doped semiconducting polymers, Nat. Mater. 20 (2021) 1414–1421. https://doi.org/10.1038/s41563-021-01008-0.

[59] V. Ugraskan, F. Karaman, Polyaniline/Graphitic Carbon Nitride Nanocomposites with Improved Thermoelectric Properties, Journal of Elec Materi 50 (2021) 3455–3461. https://doi.org/10.1007/s11664-021-08856-1.

[60] R. Nayak, P. Shetty, S. M, A. Rao, S. K V, S. Wagle, S. Nayak, V. Kamath, N. Shetty, M. Saquib, Formulation and optimization of copper selenide/PANI hybrid screen printing ink for enhancing the power factor of flexible thermoelectric generator: A synergetic approach, Ceramics International 50 (2024) 25779–25791. https://doi.org/10.1016/j.ceramint.2024.04.315.

[61] D. Venkateshvaran, M.T.R. Cervantes, L.J. Spalek, K.-H. Hwang, K. Pudzs, M. Rutkis, G. Schweicher, P. Padilla-Longoria, Understanding the Thermoelectric Transport Properties of Organic Semiconductors through the Perspective of Polarons, Adv Devices Instrum 5 (2024) 0067. https://doi.org/10.34133/adi.0067.

[62] S. Watanabe, M. Ohno, Y. Yamashita, T. Terashige, H. Okamoto, J. Takeya, Validity of the Mott formula and the origin of thermopower in π -conjugated semicrystalline polymers, Phys. Rev. B 100 (2019) 241201. https://doi.org/10.1103/PhysRevB.100.241201.

[63] J. Liu, Y. Shi, J. Dong, M.I. Nugraha, X. Qiu, M. Su, R.C. Chiechi, D. Baran, G. Portale, X. Guo, L.J.A. Koster, Overcoming Coulomb Interaction Improves Free-Charge Generation and Thermoelectric Properties for n-Doped Conjugated Polymers, ACS Energy Lett. 4 (2019) 1556–1564. https://doi.org/10.1021/acsenergylett.9b00977.

[64] M. Duhandžić, M. Lu-Dìaz, S. Samanta, D. Venkataraman, Z. Akšamija, Carrier Screening Controls Transport in Conjugated Polymers at High Doping Concentrations, Phys. Rev. Lett. 131 (2023) 248101. https://doi.org/10.1103/PhysRevLett.131.248101.